

Article

State of Health Estimation of Lithium-Ion Battery Based on Novel Health Indicators and Improved Support Vector Regression

Ruoxia Li ^{1,2,*}, Ning He ³ and Fuan Cheng ^{4,*}

¹ School of Information and Control Engineering, Xi'an University of Architecture and Technology, Xi'an 710055, China

² School of Architecture, Xi'an University of Architecture and Technology, Xi'an 710055, China

³ School of Mechanical and Electrical Engineering, Xi'an University of Architecture and Technology, Xi'an 710055, China; hening@xauat.edu.cn

⁴ School of Materials Science and Engineering, Xi'an University of Architecture and Technology, Xi'an 710055, China

* Correspondence: rli@xauat.edu.cn (R.L.); 2007110172@xauat.edu.cn (F.C.)

Abstract

Accurate estimation of the state of health (SOH) is a critical function of battery management system (BMS), essential for ensuring the safe and stable operation of lithium-ion batteries. To improve estimation precision, this paper proposes a novel health indicator (HI) construction method and an improved support vector regression (SVR) approach. First, the convolution operation is applied to discharge voltage data to extract new HIs that characterize battery aging; their correlations are then verified. Second, principal component analysis (PCA) is employed to reduce input dimensionality and computational burden. Third, to address the challenge of SVR parameter selection, an improved sparrow search algorithm (ISSA) is proposed for parameter optimization. Finally, the proposed method is validated using both the NASA dataset and a laboratory experimental dataset, with comparisons against existing approaches. The results show that the method achieves accurate SOH estimation under various aging conditions, demonstrating its effectiveness, robustness, and practical potential.



Academic Editor: Alessandro Lampasi

Received: 31 July 2025

Revised: 15 September 2025

Accepted: 17 September 2025

Published: 23 September 2025

Citation: Li, R.; He, N.; Cheng, F. State of Health Estimation of Lithium-Ion Battery Based on Novel Health Indicators and Improved Support Vector Regression. *Batteries* **2025**, *11*, 347. <https://doi.org/10.3390/batteries11100347>

Copyright: © 2025 by the authors. Licensee MDPI, Basel, Switzerland. This article is an open access article distributed under the terms and conditions of the Creative Commons Attribution (CC BY) license (<https://creativecommons.org/licenses/by/4.0/>).

1. Introduction

With rapid societal development, growing requirements for energy, fossil energy shortages, and worsening environmental deterioration are becoming increasingly serious, and all countries are actively looking for clean and efficient new energy that can replace traditional oil energy [1]. According to the white paper “China’s Energy Development in the New Era”, China will vigorously develop new energy and related industries, among which the electric vehicle is an important choice for sustainable development [2]. Lithium-ion batteries, with their high energy density, long service life, low self-discharge rate, lack of memory effect, and other excellent characteristics, have found extensive applications in electric vehicles, mobile phones, and other electronic devices [3,4]. However, their performance inevitably degrades over time due to electrode reactions and environmental factors, which may impair equipment operation or even cause safety incidents [5,6]. Effective battery management system (BMS) is therefore essential, and accurate estimation of state of health

(SOH) is a critical component. SOH estimation enables the tracking of battery aging and is fundamental to reliable and safe operation [7–9], with SOH typically defined as the ratio of current capacity to nominal capacity, i.e.,

$$SOH = \frac{Q_{current}}{Q_{nominal}} \times 100\% \quad (1)$$

Lately, numerous research studies have been performed on the SOH estimation of lithium-ion batteries, and the existing methodologies can be broadly distributed into three groups: direct measurement method, model-based method, and data-driven method [10–12]. The direct measurement method determines SOH by discharge tests, directly measuring capacity, internal resistance, or impedance. Shim et al. [13] analyzed changes in electrode properties using techniques such as impedance spectroscopy, X-ray diffraction, and atomic force microscopy, identifying causes of capacity decline. Galeotti et al. [14] applied impedance spectroscopy to four lithium-ion batteries and established a link between ohmic resistance and available capacity to estimate SOH quickly. Although this method offers high accuracy and clear principles, it is limited to laboratory settings and offline measurements.

The model-based method establishes aging mechanism models of lithium-ion batteries, expressing physical and chemical changes through equations to simulate internal reactions and degradation. Wei et al. [15] proposed an online identification battery model and used the Kalman filter and the recursive least square method to achieve dual estimation of the charging state and capacity on multiple time scales. Experimental results showed that the proposed method can estimate model parameters and the charging state and capacity in real time, with a fast convergence speed and high precision. Lyu et al. [16] introduced a novel particle filter structure by simulating the electrochemical model of the battery charge and discharge process, and the experimental verification showed that the particle filter based on the electrochemical model has higher estimation precision. However, these models are complex, require many parameters, and are difficult to construct perfectly, limiting their practical application.

Data-driven methods circumvent the complex analysis of internal aging mechanisms by directly extracting salient features from monitored battery states [17]. These approaches demonstrate high estimation accuracy and real-time capability, and they have been widely applied to SOH estimation for lithium-ion batteries. Xia et al. [18] extracted robust aging features from reconstructed voltage curves and integrated incremental capacity and differential voltage analysis with an improved BiGRU-attention model to jointly predict battery SOH and RUL. Chen et al. [19] proposed a novel deep learning framework that denoises input signals and adaptively focuses on critical multi-scale features for accurate SOH and SOC estimation under complex operating conditions. Zhao et al. [20] combined Wasserstein distance-based similarity features, voltage-position encoding, and convolutional neural networks (CNNs) to perform robust SOH estimation from incomplete charging profiles. Liu et al. [21] transformed one-dimensional charging voltage time-series data into two-dimensional representations using the Gramian angular summation field and applied ResNet for SOH estimation. Among data-driven methods, attention and transformer-based frameworks have gained wide attention in recent years. By capturing long-range dependencies and adaptively focusing on critical features, they offer strong potential for improving SOH estimation accuracy and robustness across diverse operating conditions. Gu et al. [22] and Bai et al. [23] both proposed a hybrid CNN-transformer framework for SOH prediction. They demonstrated that combining these architectures significantly improved feature representation and led to more accurate and robust SOH prediction. Zhu et al. [24] and Zhang et al. [25] both employed transformer-based architectures combined

with convolutional modules to achieve multi-feature fusion and SOH prediction. By enhancing the transformer's ability to capture local features while integrating diverse health indicators, they demonstrated an improved accuracy and robustness in lithium-ion battery SOH estimation.

In summary, although data-driven methods have made progress in SOH estimation, significant challenges remain. Existing studies often rely on health indicators (HIs) directly derived from raw voltage or capacity curves, which makes them highly sensitive to noise and external interference. Moreover, most data-driven models use parameters chosen heuristically, without systematic optimization, which weakens model generalization and prediction accuracy. As shown in Table 1, the proposed ISSA-SVR is presented alongside representative literature on recent advanced methods for comparison.

Table 1. Comparison of ISSA-SVR with recent studies.

Reference	Method	Dataset	Key Technique
Wu et al. (2023) [1]	PCA-PSO-BP neural network	NASA	Dimensionality reduction + hybrid optimization
Ma et al. (2022) [3]	Improved LSTM + HI extraction	NASA + MIT	Deep learning with handcrafted HIs
Xia et al. (2023) [18]	BiGRU + incremental capacity and DV features	CALCE + Sandia	BiFRU + attention
Zhu et al. (2024) [24]	Sparse self-attentive transformer	NASA + CALCE	Multi-feature fusion + attention + convolution
Chen et al. (2025) [19]	Multi-scale channel attention network	Lab	Multi-feature extraction + attention-based hybrid network
Zhang et al. (2025) [25]	Improved transformer with DCC	CALCE	Multi-feature extraction + transformer
This work	ISSA-SVR	NASA + Lab	Convolution-based HI + PCA + ISSA optimization

To address these gaps, this paper makes the following contributions:

1. We propose a new set of HIs extracted from voltage convolution sequences, which emphasize cycle-to-cycle morphological changes and provide robust descriptors of battery aging.
2. The extracted HIs are quantitatively analyzed for their correlation with SOH, and principal component analysis (PCA) is applied to remove redundancy and reduce model input complexity.
3. An improved sparrow search algorithm (ISSA) is developed to optimize the critical parameters of a support vector regression (SVR) model, enhancing both robustness and accuracy in SOH estimation.

In addition, the work also provides new insight into battery degradation modeling by showing that convolution-based indicators capture electrochemical aging signatures embedded in voltage profiles, and by demonstrating how metaheuristic-regression integration can effectively represent the inherently nonlinear trajectory of SOH evolution.

2. Battery Data Analysis and Feature Extraction

In this paper, two battery datasets are used to verify the proposed SOH estimation method. One is the NASA dataset from the PCOE Research Center [26]. The other is the T1 and T2 battery dataset obtained from controlled laboratory aging experiments.

2.1. Battery Aging Dataset Description

The NASA dataset consists of 18,650 lithium-ion batteries with a nominal capacity of 2 Ah, tested under an ambient temperature of 24 °C. During the experiments, the batteries were charged at a constant current of 1.5 A until the terminal voltage reached 4.2 V, followed by constant-voltage charging until the current decreased to 20 mA. Throughout this process, terminal voltage, charging temperature, charging current, and time data were recorded. The discharge process was then performed at a constant current of 2 A until the terminal voltage reached the cut-off limit, at which point terminal voltage, discharge temperature, discharge current, time, and battery capacity were measured. The experimental information on this dataset is summarized in Table 2, and the corresponding capacity degradation curve is shown in Figure 1.

Table 2. Battery experiment data information.

Label	Temperature/°C	Charging Current/A	Discharge Current/A	Cut-Off Voltage/V
B5				2.7
B6				2.5
B7	24	1.5		2.2
B18			2	2.5

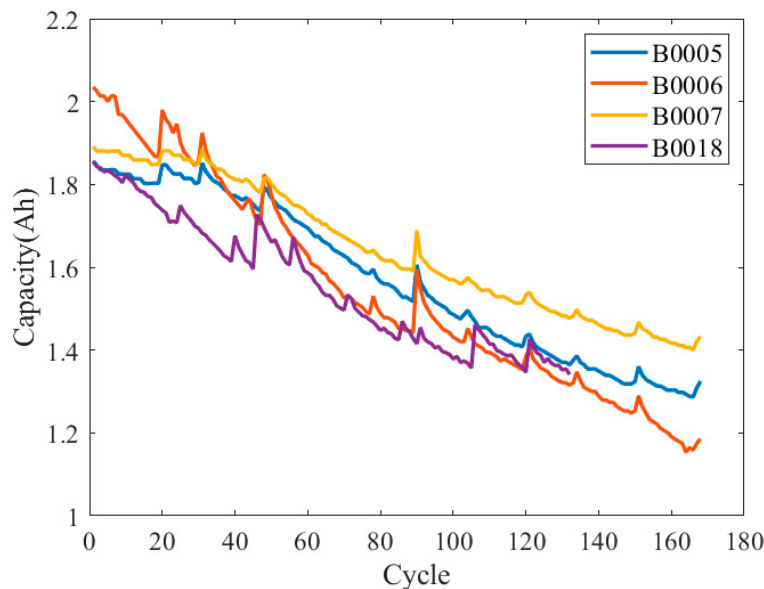


Figure 1. Capacity degradation curves of four batteries in NASA dataset.

The second dataset used in this study was obtained from a laboratory charge–discharge test platform, with the experimental setup illustrated in Figure 2. The platform consists of an MHW-200 constant-temperature test chamber developed by Newell Laboratories, a battery charge–discharge test channel, and a computer system for real-time monitoring and data acquisition. The test objects are two standard 18,650-type lithium-ion cells with LiCoO₂ cathodes and graphite anodes, with detailed specifications provided in Table 3. The experiments employed a constant-current charging, constant-voltage charging, and constant-current discharging protocol at an ambient temperature of 24 °C, and the corresponding data were recorded throughout the aging process. The experimental details are summarized in Table 4, and the capacity degradation curve is shown in Figure 3. Note that parameters such as ambient temperature, charge/discharge current, and voltage thresholds were precisely regulated for all experiments to isolate cycle-based aging.

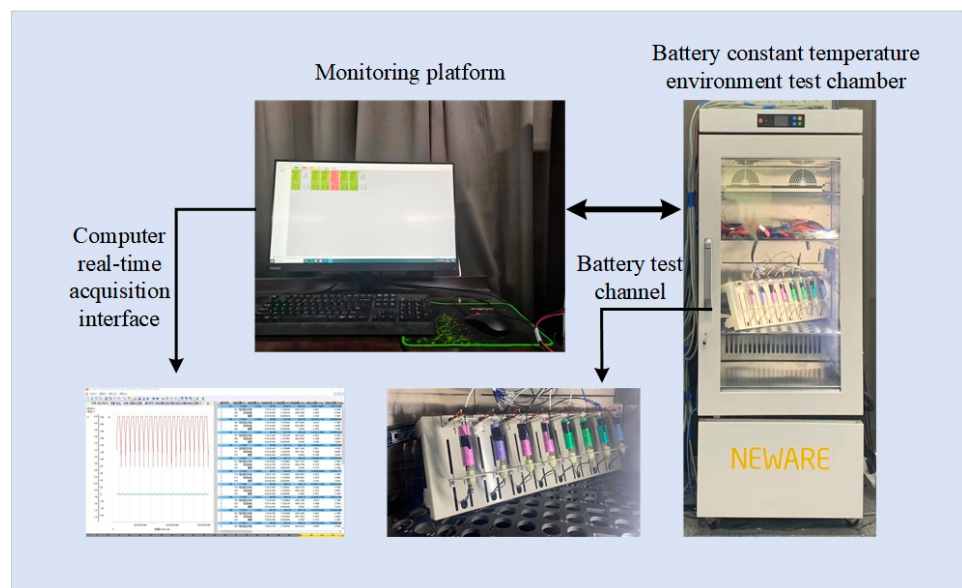


Figure 2. Lab battery testing platform.

Table 3. Specifications of experimental batteries.

Battery	Capacity (Ah)	Nominal Voltage (V)	Working Voltage (V)	Internal Resistance (mΩ)	Weight (g)	Dimension (mm)
T1	3	3.7	2.7–4.2	12	46	18 × 65
T2	2.6	3.7	2.7–4.2	12	46	18 × 65

Table 4. Battery experiment procedures.

Step	Step Name	Work Time	Voltage/V	Current/mA	Cut-Off Voltage/V	Cut-Off Current/mA
1	Constant-current—constant-voltage charging	/	4.2	1500	/	20
2	Constant-current discharging	/	/	2000	2.7	/
3	Rest	5 min	/	/	/	/
4	Cycle	Start step: 1	/	/	/	/
5	End	/	/	/	/	/

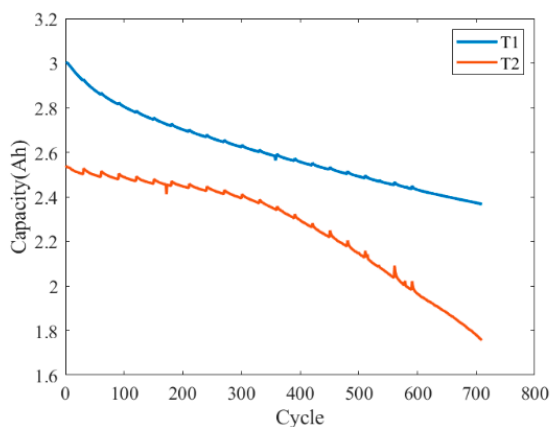


Figure 3. Capacity degradation curves of two batteries in laboratory dataset.

2.2. Feature Extraction

Extracting appropriate HIs that accurately reflect the SOH of a battery is a critical step in data-driven methods, as it directly affects the estimation precision of the model. Using the B0018 battery as a case study, the novel HI extraction process proposed in this paper is illustrated in Figure 4. Since the charging process is generally more controlled, HIs are extracted from the discharge process. In each charge–discharge cycle, the discharge voltage decreases gradually at first and then more rapidly; with an increasing cycle number, the rate at which the terminal voltage reaches the cut-off threshold also accelerates. To capture this degradation behavior, discharge voltage was selected as the basis for HI extraction. Because raw data collection is susceptible to external noise, a convolution operation was applied to two adjacent discharge voltage sequences to enhance feature extraction. As shown in Figure 4, the convolution sequence exhibits clear trends as cycling progresses, with the span, peak value, and peak horizontal coordinate gradually all decreasing. Based on this observation and analysis, nine HIs were selected to characterize battery aging: span value, integral value, kurtosis, peak value, peak abscissa coordinate, peak slope, fuzzy entropy, energy value, and variance.

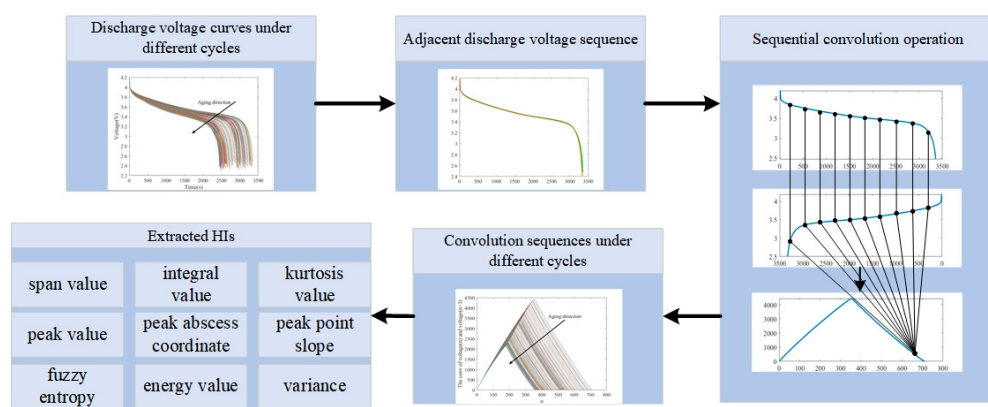


Figure 4. HI extraction process.

Convolution-based methods, particularly CNNs and their variants, have been widely applied in signal-processing-related areas to address problems such as noise suppression, feature extraction, and information enhancement [27–30]. The convolution operation describes the process by which two functions or sequences produce a third function or sequence by a specific integration or summation operation, expressed as

$$y(n) = (x * h)(n) = \sum_{m=-\infty}^{+\infty} x(m)h(n-m) \quad (2)$$

The convolution operation has translation invariance, meaning that the extracted features remain valid regardless of their position in the input sequence. By focusing on local regions rather than the entire sequence, convolution provides spatial locality, which improves efficiency and makes it well suited for processing long input data. In addition, convolution acts as a smoothing and filtering mechanism. It suppresses high-frequency noise and highlights low-frequency trends that are closely related to gradual battery degradation. This allows the method to emphasize nonlinear aging patterns and makes aging-related patterns more distinguishable than in raw voltage profiles.

In addition, Pearson correlation coefficient (PCC) is utilized to evaluate the correlation between extracted HIs and battery SOH, and its expression is shown as follows:

$$PCC = \frac{\sum_{i=1}^n (z_i - \bar{z})(q_i - \bar{q})}{\sqrt{\sum_{i=1}^n (z_i - \bar{z})^2} \sqrt{\sum_{i=1}^n (q_i - \bar{q})^2}} \quad (3)$$

where z and q represent HIs and SOH, respectively.

The PCC value range is within $[-1, 1]$. As the absolute value approaches 1, the correlation becomes stronger. PCC values for each battery are presented in Figure 5. It is notable that the worst correlation between HIs extracted in this paper and battery SOH is between 0.6 and 0.8, indicating a strong correlation between variables, and the rest are above 0.8, indicating an extremely strong correlation between variables. That is, the nine extracted HIs can effectively represent the battery degradation, which proves the rationality and effectiveness of the feature selection.

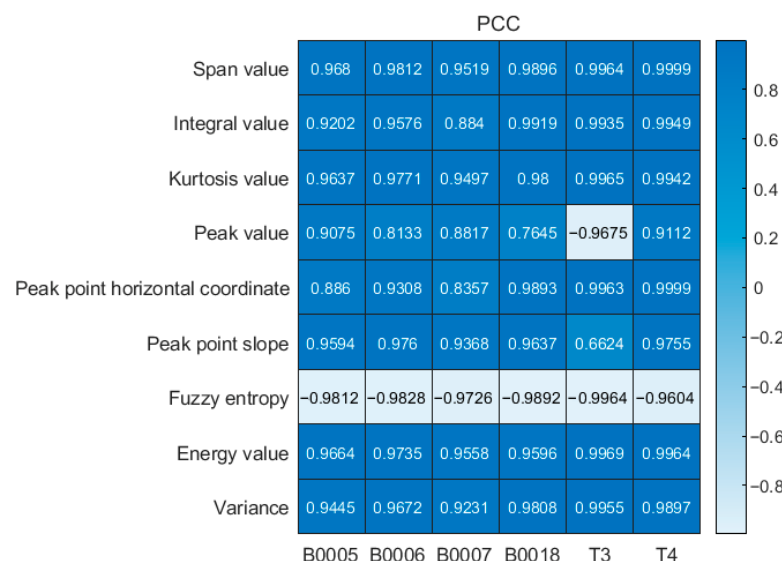


Figure 5. Pearson correlation coefficient results for each battery.

2.3. HI Optimization

2.3.1. PCA-Based Dimensionality Reduction Method

Considering the computational burden of the ISSA-SVR model and the presence of linear correlations among certain HIs, which leads to information redundancy, it is necessary to optimize the extracted HIs. PCA is a statistical analysis technique used for data compression and feature extraction. It uses orthogonal transformation to convert a group of correlated factors into a group of independent new factors, which can not only effectively reduce the data dimension but also retain relatively important information in the original data and reduce the complexity of the data [31,32]. The primary calculation processes of PCA are as described next.

Suppose there are n p-dimensional data $x_j = (x_{j1}, x_{j2}, \dots, x_{jp})^T, j = 1, 2, \dots, n$, construct a standardized sample matrix:

$$Z_{ij} = \frac{x_{ij} - \bar{x}_j}{s_j}, i = 1, 2, \dots, n; j = 1, 2, \dots, p \quad (4)$$

$$\bar{x}_j = \frac{\sum_{i=1}^n x_{ij}}{n}, s_j = \sqrt{\frac{\sum_{i=1}^n (x_{ij} - \bar{x}_j)^2}{n-1}} \quad (5)$$

Calculate the correlation coefficient matrix R for the standardized matrix Z :

$$R = \frac{Z^T Z}{n - 1} \quad (6)$$

Solve the characteristic equation of the correlation coefficient matrix R to determine its principal components:

$$|R - \lambda I_p| = 0 \quad (7)$$

$$\frac{\sum_{j=1}^p \lambda_j}{\sum_{j=1}^p \lambda_j} \geq \delta \quad (8)$$

where δ is the threshold for the sum of the contributions of the principal components, p , which can be determined through δ .

The unit eigenvector b_j^o is obtained by solving the following equation:

$$Rb = \lambda_j b \quad (9)$$

Convert standardized variables to principal components:

$$U_{ij} = z_i^T b_j^o, j = 1, 2, \dots, p \quad (10)$$

2.3.2. HIs Optimization Results

The extracted HIs are optimized according to PCA, revealing the contribution percentages of individual principal components, as detailed in Table 5. The total contribution rates of the first two principal components of each battery are 98.41%, 97.70%, 97.95%, 98.46%, 99.39%, and 99.92%, respectively. Generally speaking, if the contribution rate of the principal components reaches 97%, it means that it is sufficient to describe the characteristic information contained in the original data. In other words, the first two principal components of each battery can be used as HIs reflecting the battery aging phenomenon, which significantly reduces the input size of the model and is conducive to the subsequent SOH estimation work.

Table 5. Contribution rates of each principal component.

3. ISSA-SVR Method

3.1. Support Vector Regression

Support vector machine (SVM) is a linear classifier based on the maximum margin principle, which identifies an optimal hyperplane for data separation [33]. For regression tasks, it is extended as support vector regression (SVR), which seeks an optimal regression hyperplane that fits the data within a narrow margin while minimizing deviations [34]. Given the nonlinear characteristics of lithium-ion battery capacity data, SVR is well-suited to SOH estimation. It reduces prediction error, is robust to outliers, and demonstrates a strong generalization ability, making it effective for nonlinear regression problems [35,36].

Assume a given sample set $S = \{x_i, y_i\}^n$ ($x_i \in X = R^n, y_i \in Y = R$), where x_i is the i th input eigenvector, y_i is the corresponding output vector, and n is the number of samples. Mapping the sample set from a low-dimensional space to a high-dimensional space through nonlinear mapping is defined as follows:

$$f(x) = w \cdot \phi(x) + b \quad (11)$$

where x is the input data; $\phi(x)$ is the nonlinear mapping function; w is the weight; and b is the intercept.

Following the structural risk minimization principle, determining $f(x)$ equates to solving an optimization task:

$$\frac{1}{2} \|w\|^2 + C \sum_i^n L(f(x_i), y_i) \quad (12)$$

where L is the loss function; and C is the penalty factor.

Introducing the insensitive loss function $\epsilon (\epsilon > 0)$ yields

$$L(f(x), y) = \begin{cases} 0, |f(x) - y| \leq \epsilon \\ |f(x) - y| - \epsilon, |f(x) - y| > \epsilon \end{cases} \quad (13)$$

Then, the SVR expression is

$$f(x) = w \cdot \phi(x) + b = \sum_i^n (\alpha_i - \hat{\alpha}_i) K(x_i, x) + b \quad (14)$$

where α_i and $\hat{\alpha}_i$ are Lagrange multipliers; and $K(x_i, x)$ is the kernel function, of which four main types are commonly used: linear kernel function, polynomial kernel function, sigmoid kernel function, and radial basis kernel function (RBF). Among them, RBF kernel function has fewer parameters and can realize high-dimensional mapping, and so it is the most commonly used kernel function [37]. Therefore, this paper chooses RBF as the kernel function of SVR, which is stated as follows:

$$K_{RBF}(x_i, x) = \exp\left(-\frac{1}{2\sigma^2} \|x_i - x\|^2\right) \quad (15)$$

where σ is the width coefficient of RBF.

The penalty factor C and kernel parameter σ impact the generalization and fitting performance of the SVR model directly, but there is no effective method to guide the parameter selection, so to acquire an accurate SVR prediction model, it is essential to optimize the parameters of SVR.

3.2. Sparrow Search Algorithm

The sparrow search algorithm (SSA), proposed by Xue and Shen in 2020, is a population-based metaheuristic with a strong optimization ability, fast convergence, and high robustness compared to many other swarm algorithms [38]. Inspired by the foraging and anti-predation behavior of sparrows, the population is divided into three roles: discoverers, joiners, and scouters. Discoverers, with higher energy reserves, guide the search for food sources, while joiners follow their paths. A small proportion act as scouters, issuing warnings when threats appear. Although individual roles may change during the search process, the proportions of discoverers and joiners remain constant. The main steps of SSA are summarized as follows:

Step 1: Population initialization.

$$X = lb + rand * (ub - lb) \quad (16)$$

where ub and lb symbolize the maximum and minimum position boundaries of the population, respectively.

Step 2: Update the discoverer position.

$$x_{i,j}^{t+1} = \begin{cases} x_{i,j}^t \cdot \exp\left(\frac{-i}{\alpha \cdot iter_{max}}\right), & R_2 < ST \\ x_{i,j}^t + Q \cdot L, & R_2 \geq ST \end{cases} \quad (17)$$

where α is a random number of $[0, 1]$; $iter_{max}$ is the maximum iteration quantity; Q is a random number obeying a normal distribution; R_2 is a random number of $[0, 1]$ and denotes the warning value; ST is a random number of $[0.5, 1]$ and denotes the safety value; and L is a one-row, j -dimensional, all-1 matrix.

Step 3: Update the joiner position.

$$x_{i,j}^{t+1} = \begin{cases} Q \cdot \exp\left(\frac{x_{worst}^t - x_{i,j}^t}{i^2}\right), & i > \frac{n}{2} \\ x_p^{t+1} + \left| x_{i,j}^t - x_p^{t+1} \right| \cdot A^+ \cdot L, & otherwise \end{cases} \quad (18)$$

where A is a $1 \times d$ matrix with elements randomly assigned 1 or -1 ; and $A^+ = A^T (AA^T)^{-1}$.

Step 4: Scouter and early warning.

$$x_{i,j}^{t+1} = \begin{cases} x_{best}^t + \beta \cdot (x_{i,j}^t - x_{best}^t), & f_i \neq f_g \\ x_{i,j}^t + K \left(\frac{x_{i,j}^t - x_{worst}^t}{|f_i - f_w| + \varepsilon} \right), & f_i = f_g \end{cases} \quad (19)$$

where β is a random number obeying a normal distribution with mean 0 and variance 1; K is a random number of $[-1, 1]$, with the positive and negative indicating the orientation the sparrow is moving, and the size indicating the step control parameter; f_i denotes the current individual fitness value; and f_g denotes the current minimum fitness value.

Step 5: Calculate the fitness value and adjust the sparrow location.

Step 6: Verify if the stopping criterion is fulfilled—if so, output the optimal sparrow position; otherwise, return to step 2.

3.3. Improved Sparrow Search Algorithm

The traditional SSA can effectively search small solution spaces and often finds good local optima due to its strong local search ability. It is simple, easy to understand, and straightforward to implement. However, it suffers from slow convergence, a weak global search capability, and a tendency to become trapped in local minima. To address these limitations, this paper proposes an improved SSA (ISSA), which enhances population

diversity and global exploration, enabling the algorithm to escape local optima and achieve higher convergence accuracy.

Chaotic mapping is introduced to initialize the population due to its advantages over random initialization. The original SSA often suffers from low population diversity, while chaotic mapping exhibits high complexity and stochasticity as a nonlinear process. Using them instead of conventional random methods can yield more stochastic sequences, leading to a more uniform population distribution, improved ergodicity, and enhanced global search ability [39]. Thus, Bernoulli mapping is employed to initialize the population, given by

$$z_{k+1} = \begin{cases} z_k / (1 - \rho), & z_k \in (0, 1 - \rho] \\ (z_k - 1 + \rho) / \rho, & z_k \in (1 - \rho, 1) \end{cases} \quad (20)$$

where k is the number of chaotic iterations; and ρ is a control parameter.

The sine–cosine algorithm (SCA) is introduced to enhance the discoverer position update in the SSA. In the SSA, the discoverer guides joiners toward food sources. However, if the discoverer becomes trapped in a local optimum, it may lead numerous joiners to converge prematurely, causing population stagnation and increasing the risk of local convergence. The SCA, proposed by Mirjalili in 2016 [40], is a stochastic optimization method that utilizes sine and cosine functions for an oscillatory search. It is characterized by simplicity, few parameters, and ease of implementation. In this work, the SCA is incorporated to modify Equation (17) in the SSA, enabling balanced global exploration and local exploitation through adaptive sine–cosine oscillations. The improved equation is as follows:

$$x_{i,j}^{t+1} = \begin{cases} w \cdot x_{i,j}^t + r_1 \cdot \sin(r_2) \cdot |r_3 \cdot x_{best}^t - x_{i,j}^t|, & R_2 < ST \\ w \cdot x_{i,j}^t + r_1 \cdot \cos(r_2) \cdot |r_3 \cdot x_{best}^t - x_{i,j}^t|, & R_2 \geq ST \end{cases} \quad (21)$$

$$w = \frac{e^{\frac{t}{iter_{max}}} - 1}{e - 1} \quad (22)$$

$$r_1 = a(1 - \frac{t}{T}) \quad (23)$$

where a is a constant, usually set to 1 or 2; t is the number of current iterations; T is the maximum number of iterations; and r_2, r_3 are random numbers of $[0, 2\pi]$, which control the travel distance of sparrows and the effect of the optimal individual on the last position of sparrows, respectively. The improved expression can maintain the individual diversity and enhance the global search capability of the algorithm by applying the oscillation change characteristic of the sine–cosine model to the particle position.

To mitigate premature convergence and limited diversity caused by joiners closely following discoverers in the SSA, a spiral search strategy from the whale optimization algorithm [41] is introduced. This dynamic update mechanism enhances movement flexibility, thereby improving population diversity, search efficiency, and optimization accuracy [42]. Accordingly, Equation (18) in the SSA is modified as follows:

$$x_{i,j}^{t+1} = \begin{cases} \cos(2\pi l) \cdot Q \cdot \exp(\frac{x_{worst}^t - x_{i,j}^t}{l^2} + z \cdot l), & i > \frac{n}{2} \\ x_p^{t+1} + |x_{i,j}^t - x_p^{t+1}| \cdot A^+ \cdot L \cdot e^{zl} \cdot \cos(2\pi l), & otherwise \end{cases} \quad (24)$$

$$z = e^{k \cos[\pi(1 - \frac{i}{i_{max}})]} \quad (25)$$

where k is the change coefficient; and l is a uniformly distributed random number in $[-1, 1]$.

Owing to its stability and strong approximation properties, Gaussian perturbation exhibits an excellent local search performance. Applying this strategy to global-best indi-

viduals in the SSA facilitates an escape from local optima and enhances global exploration. The Gaussian perturbation is defined as follows:

$$x_{g\text{best}}^t = x_{\text{best}}^t \cdot (1 + \text{Gaussian}(u, \sigma^2)) \quad (26)$$

where x_{best}^t is the current global optimal individual; $x_{g\text{best}}^t$ is the global optimal entity after Gaussian perturbation; u is the mean value of a Gaussian distribution; and σ is the standard deviation of the distribution.

3.4. ISSA-SVR

In this paper, the ISSA is employed to optimize the penalty factor C and kernel parameter σ in SVR, so as to enhance the estimation precision of the model. Compared with the original SSA, the ISSA can not only effectively prevent the SSA from falling into local optima but also enhance the rate of convergence and optimization precision of the SSA. In the ISSA-SVR model, the mean square error (MSE) is taken as its fitness function, and its expression is as follows:

$$\text{fitness} = \text{MSE} = \frac{1}{N} \sum_{i=1}^N (y_i - \hat{y}_i)^2 \quad (27)$$

where N is the number of training samples; y_i is the actual value of the i th training sample; and \hat{y}_i is the predicted value of the i th training sample. The main parameters of the ISSA-SVR are described in Table 6.

Table 6. ISSA-SVR parameters.

Parameter	Meaning	Value
N	Population size	100
T	Max. iterations	20
k	Number of chaotic iterations	100
ρ	Control parameter	0.7
C	Penalty	16
γ	RBF width	0.01

ISSA-SVR steps are described as follows:

- (1) Data preprocessing: Normalized processing of input data, specifically expressed as

$$x_{\text{norm}} = \frac{x_i - x_{\min}}{x_{\max} - x_{\min}} \quad (28)$$

where x_{norm} denotes the normalized data; x_i denotes the original data; and x_{\min} and x_{\max} are the minimum and maximum values of the original data, respectively.

- (2) Initialization: Set parameters such as population size, maximum iteration threshold, quantity of discoverers, boundaries for initial value ranges, and dimension of independent variables.
- (3) Population Initialization: Initialize individual positions using Bernoulli chaotic mapping (Equation (20)).
- (4) Fitness Evaluation and Ranking: Compute each individual's fitness via the objective function (Equation (27)), and then rank all individuals and assign the best as discoverers, others as joiners.
- (5) Position Update: Update the position of the discoverers based on Equations (21)–(23); update the position of the joiners based on Equations (24) and (25); update the individual positions of the scouter and early warning based on Equation (19).

- (6) Fitness Update: Recompute fitness values and update the best and worst fitness records and their positions.
- (7) Gaussian Perturbation: Apply Gaussian mutation (Equation (26)) to the global-best individual to avoid local optima.
- (8) Termination Check: Output results if the stopping criterion is met; otherwise, return to Step 4.

The pseudo-code for the ISSA-SVR algorithm (Algorithm 1) is shown below.

Algorithm 1. ISSA-SVR

Inputs: Population size pop , the maximum iterations M , the number of discoverers PN , the number of scouter SN

Outputs: global optimal location $bestx$, global optimal fitness f_g

1. Initialize population individual positions according to the Bernoulli mapping based on Equation (20).
 2. **for** $t = 1: M$ **do**
 - a. Calculate the fitness value of an individual and find the minimum fitness value f_g and maximum fitness value f_w based on Equation (27);
 - b. Rank Individuals, select the top PN individuals as discoverers the rest as joiners;
 - c. Update the position of the discoverers (Equations (21)–(23)), joiners (Equations (24) and (25)) and scouter (Equation (19)).
 - d. Calculate the current individual fitness value and update $f_g, f_w, bestx$.
 - e. Apply Gaussian perturbation to global best solution based on Equation (26).
 3. **End for**
 4. **Return** $bestx$ and f_g
-

The block diagram of the proposed SOH estimation approach is displayed in Figure 6. As illustrated in the figure, the suggested approach is roughly separated into four components: data acquisition, feature extraction and processing, model training and SOH estimation, and error analysis. Firstly, discharge voltage data from the NASA battery dataset and the actual laboratory battery dataset are collected. Secondly, convolution operations are carried out on adjacent voltage sequences, respectively, and nine HIs are extracted from the resulting convolution sequences, and the correlation between them and the battery capacity are verified. To diminish the computational burden of the model, PCA is utilized to optimize dimensionality reduction in the extracted HIs. Then, ISSA is employed to optimize parameters in the SVR model, and HIs after dimensionality reduction and battery capacity data are divided into the training set and the testing set. The training set is utilized to train the ISSA-SVR model offline, and the testing set is utilized to test the SOH estimation accuracy of the model online. Finally, four error indicators are employed to assess the estimation performance of the suggested approach.

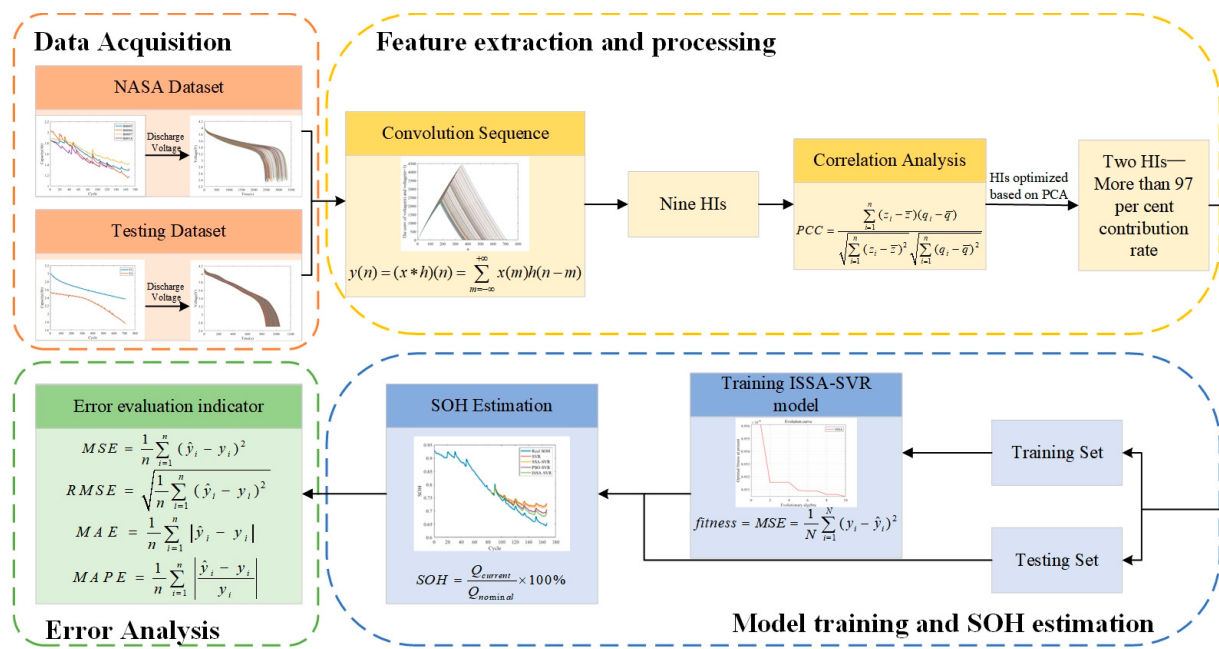


Figure 6. SOH estimation framework of the proposed method.

4. Experimental Results and Analysis

4.1. Error Evaluation Indicator

To more accurately evaluate the performance of the proposed SOH estimation approach, several error metrics are employed, including mean square error (MSE), root mean square error (RMSE), mean absolute error (MAE), and mean absolute percentage error (MAPE). Their mathematical expressions are given as follows:

$$MSE = \frac{1}{n} \sum_{i=1}^n (\hat{y}_i - y_i)^2 \quad (29)$$

$$RMSE = \sqrt{\frac{1}{n} \sum_{i=1}^n (\hat{y}_i - y_i)^2} \quad (30)$$

$$MAE = \frac{1}{n} \sum_{i=1}^n |\hat{y}_i - y_i| \quad (31)$$

$$MAPE = \frac{1}{n} \sum_{i=1}^n \left| \frac{\hat{y}_i - y_i}{y_i} \right| \quad (32)$$

where y_i is the true value of SOH under the i th cycle; \hat{y}_i is the SOH estimate value under the i th cycle; and n is the total number of cycles evaluated by SOH.

4.2. Ablation Experiments

To verify the effectiveness of the proposed modules in ISSA-SVR, we conducted ablation experiments on both PCA-based dimensionality reduction and the ISSA refinements, namely, Bernoulli chaotic mapping (BM), the SCA, spiral search (PSA), and Gaussian perturbation (GP). For PCA, Tables 7 and 8 show that removing PCA increases both the training time and MSE, confirming that dimensionality reduction significantly improves computational efficiency and predictive accuracy. For the ISSA refinements, Tables 9 and 10 show that the complete ISSA-SVR consistently achieves the fastest convergence and lowest error, while removing individual modules leads to a degraded performance, with the most notable deterioration observed when SCA and PSA are excluded. These findings

demonstrate that PCA effectively reduces redundancy in high-dimensional data, while the ISSA refinements collectively enhance the convergence speed, accuracy, and robustness, thereby validating the necessity of each proposed component.

Table 7. Results of ablation experiments of PCA on B0005 dataset.

Method	ISSA-SVR	w/o PCA
Training time(s)	80	89
MSE	0.00042	0.00071

Table 8. Results of ablation experiments of PCA on T3 dataset.

Method	ISSA-SVR	w/o PCA
Training time(s)	110	125
MSE	0.00007	0.00015

Table 9. Results of ablation experiments of ISSA modules on B0005 dataset.

Method	ISSA-SVR	w/o BM	w/o SCA	w/o PSA	w/o GP
Convergence iterations	45	49	57	49	45
MSE	0.00042	0.00050	0.00057	0.00048	0.00049

Table 10. Results of ablation experiments of ISSA modules on T3 dataset.

Method	ISSA-SVR	w/o BM	w/o SCA	w/o PSA	w/o GP
Convergence iterations	34	43	52	39	39
MSE	0.00007	0.00009	0.00013	0.00011	0.00008

4.3. Estimation Results and Analysis

Based on the NASA battery dataset and the laboratory battery dataset, this section analyzes and discusses the estimation performance of the proposed ISSA-SVR method. To evaluate robustness under different data conditions, 50%, 60%, and 70% of each dataset is used as a training set, and the results are compared against SVR, SSA-SVR, and PSO-SVR under the same training protocols. The SOH estimation results of the four models for each battery are displayed in Figures 7–12. As shown in the figures, under different training modes, the SOH estimation performance improves as the training set proportion increases. For the same training ratio, the SVR model shows a poor generalization ability and the largest prediction errors. Although SSA-SVR and PSO-SVR improve the estimation accuracy to some extent, their overall performance remains suboptimal. In contrast, the proposed ISSA-SVR achieves the highest accuracy and the closest alignment with the actual SOH degradation curve, confirming its precision and robustness in SOH estimation.

The error metrics of different models across various batteries are shown in Tables 11 and 12 below. It can be observed that the values of MSE, RMSE, MAE, and MAPE of the proposed approach are all within 4%, with MSE consistently below 0.1%, demonstrating its strong performance in SOH estimation. Taking the B0005 battery of the 50% training set as an example, the MSE value of the ISSA-SVR method reduces the MSE by 77.78%, 73.33%, and 50.00% compared with SVR, SSA-SVR, and PSO-SVR, respectively. Similarly, the RMSE value is reduced by 50.71%, 45.99%, and 24.28%; the MAE value reduced by 50.00%, 45.32%, and 24.27%; and the MAPE value reduced by 50.00%, 45.27%, and 24.15%, respectively. These results indicate that the proposed ISSA-SVR maintains high stability across different battery datasets and provides superior accuracy and generalization compared with alternative methods.

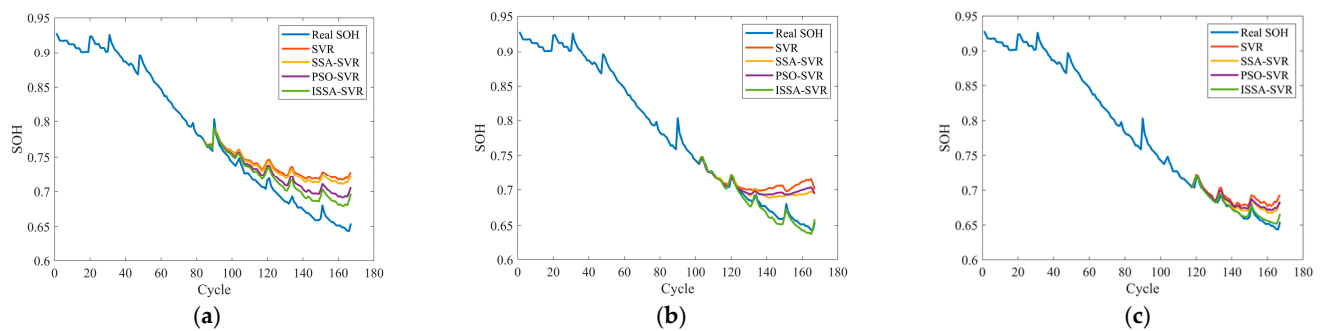


Figure 7. SOH estimation results for B0005. (a) Estimates based on 50% training set. (b) Estimates based on 60% training set. (c) Estimates based on 70% training set.

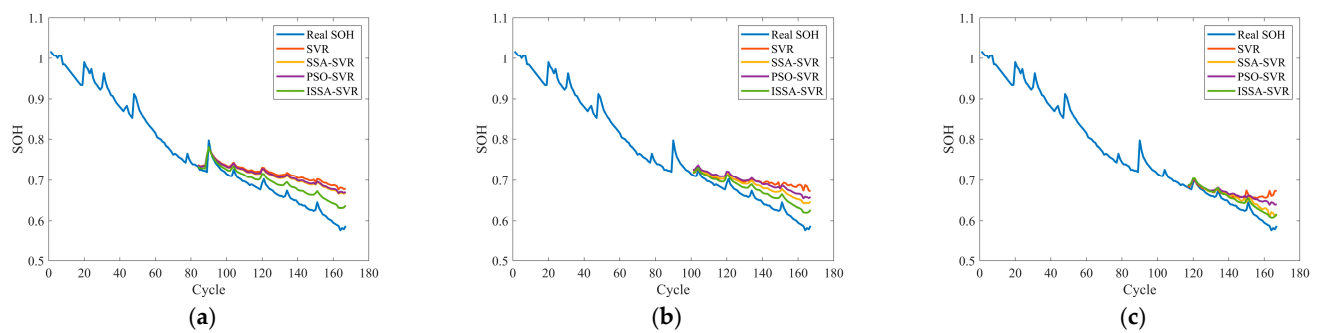


Figure 8. SOH estimation results for B0006. (a) Estimates based on 50% training set. (b) Estimates based on 60% training set. (c) Estimates based on 70% training set.

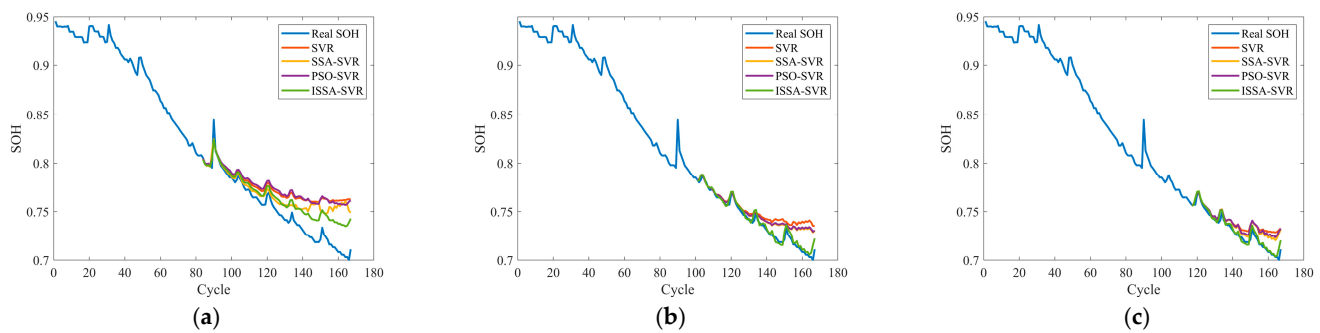


Figure 9. SOH estimation results for B0007. (a) Estimates based on 50% training set. (b) Estimates based on 60% training set. (c) Estimates based on 70% training set.

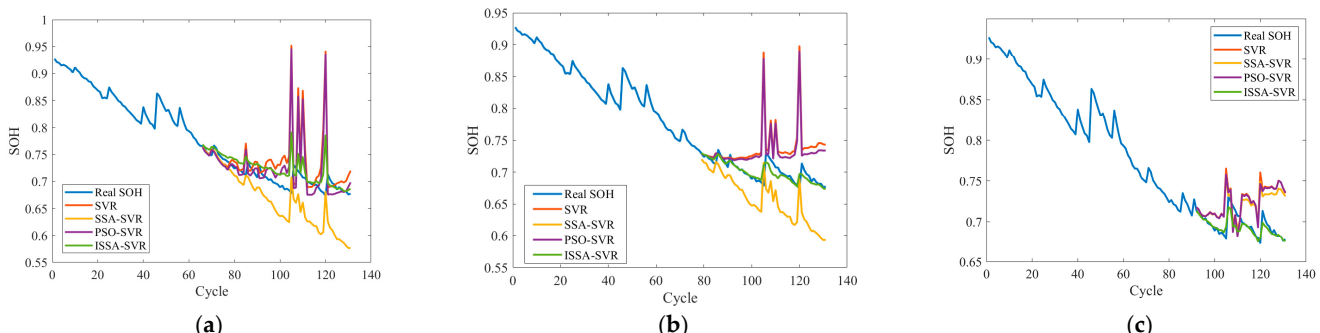


Figure 10. SOH estimation results for B0018. (a) Estimates based on 50% training set. (b) Estimates based on 60% training set. (c) Estimates based on 70% training set.

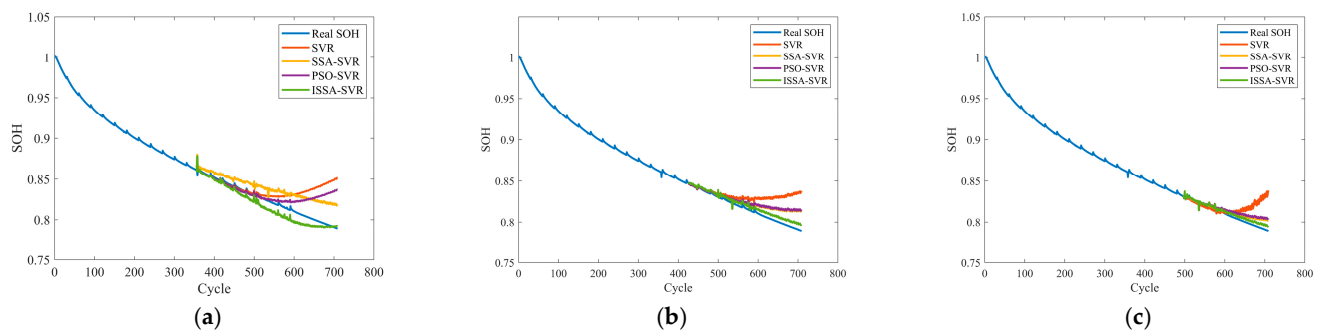


Figure 11. SOH estimation results for T3. (a) Estimates based on 50% training set. (b) Estimates based on 60% training set. (c) Estimates based on 70% training set.

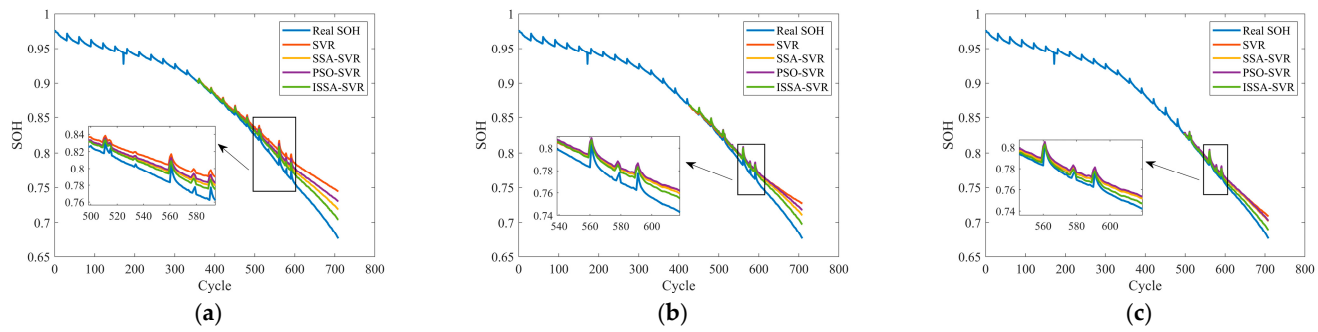


Figure 12. SOH estimation results for T4. (a) Estimates based on 50% training set. (b) Estimates based on 60% training set. (c) Estimates based on 70% training set.

Table 11. Comparison of error indicators of four models based on the NASA dataset.

Battery	Method	MSE	RMSE	MAE	MAPE
B0005 (50%)	ISSA-SVR	0.0004	0.0209	0.0181	0.0267
	SSA-SVR	0.0015	0.0387	0.0331	0.0488
	PSO-SVR	0.0008	0.0276	0.0239	0.0352
	SVR	0.0018	0.0424	0.0362	0.0534
B0005 (60%)	ISSA-SVR	0.00003	0.0055	0.0046	0.0068
	SSA-SVR	0.0005	0.0232	0.0167	0.0252
	PSO-SVR	0.0007	0.0258	0.0183	0.0277
	SVR	0.0010	0.0320	0.0232	0.0350
B0005 (70%)	ISSA-SVR	0.00002	0.0041	0.0031	0.0046
	SSA-SVR	0.0002	0.0125	0.0106	0.0158
	PSO-SVR	0.0002	0.0145	0.0114	0.0173
	SVR	0.0004	0.0193	0.0154	0.0233
B0006 (50%)	ISSA-SVR	0.0008	0.0285	0.0249	0.0387
	SSA-SVR	0.0023	0.0475	0.0413	0.0645
	PSO-SVR	0.0024	0.0492	0.0429	0.0669
	SVR	0.0030	0.0549	0.0479	0.0747
B0006 (60%)	ISSA-SVR	0.0006	0.0244	0.0224	0.0353
	SSA-SVR	0.0014	0.0370	0.0338	0.0533
	PSO-SVR	0.0021	0.0459	0.0420	0.0662
	SVR	0.0027	0.0523	0.0439	0.0701
B0006 (70%)	ISSA-SVR	0.0003	0.0171	0.0156	0.0250
	SSA-SVR	0.0005	0.0216	0.0190	0.0306
	PSO-SVR	0.0010	0.0320	0.0267	0.0434
	SVR	0.0015	0.0389	0.0290	0.0476

Table 11. Cont.

Battery	Method	MSE	RMSE	MAE	MAPE
B0007 (50%)	ISSA-SVR	0.0003	0.0171	0.0140	0.0191
	SSA-SVR	0.0006	0.0237	0.0171	0.0236
	PSO-SVR	0.0008	0.0286	0.0236	0.0322
	SVR	0.0008	0.0289	0.0229	0.0314
B0007 (60%)	ISSA-SVR	0.00002	0.0039	0.0029	0.0039
	SSA-SVR	0.0002	0.0124	0.0089	0.0124
	PSO-SVR	0.0008	0.0286	0.0236	0.0322
	SVR	0.0003	0.0160	0.0116	0.0161
B0007 (70%)	ISSA-SVR	0.00001	0.0037	0.0027	0.0037
	SSA-SVR	0.0001	0.0101	0.0080	0.0111
	PSO-SVR	0.0002	0.0129	0.0093	0.0130
	SVR	0.0002	0.0128	0.0100	0.0140
B0018 (50%)	ISSA-SVR	0.0006	0.0249	0.0155	0.0222
	SSA-SVR	0.0031	0.0560	0.0462	0.0661
	PSO-SVR	0.0032	0.0570	0.0282	0.0405
	SVR	0.0038	0.0168	0.0329	0.0473
B0018 (60%)	ISSA-SVR	0.00008	0.0090	0.0061	0.0087
	SSA-SVR	0.0022	0.0468	0.0384	0.0550
	PSO-SVR	0.0026	0.0510	0.0320	0.0465
	SVR	0.0031	0.0556	0.0367	0.0533
B0018 (70%)	ISSA-SVR	0.00007	0.0082	0.0052	0.0074
	SSA-SVR	0.0012	0.0342	0.0277	0.0402
	PSO-SVR	0.0014	0.0378	0.0308	0.0447
	SVR	0.0015	0.0391	0.0314	0.0457

Table 12. Comparison of error indicators of four models based on the laboratory dataset.

Battery	Method	MSE	RMSE	MAE	MAPE
T3 (50%)	ISSA-SVR	0.00007	0.0082	0.0070	0.0086
	SSA-SVR	0.0003	0.0168	0.0150	0.0184
	PSO-SVR	0.0003	0.0173	0.0110	0.0136
	SVR	0.0006	0.0242	0.0157	0.0196
T3 (60%)	ISSA-SVR	0.00002	0.0046	0.0041	0.0051
	SSA-SVR	0.0001	0.0109	0.0082	0.0102
	PSO-SVR	0.0001	0.0115	0.0088	0.0110
	SVR	0.0005	0.0213	0.0159	0.0199
T3 (70%)	ISSA-SVR	0.00001	0.0035	0.0030	0.0037
	SSA-SVR	0.00003	0.0055	0.0042	0.0053
	PSO-SVR	0.00005	0.0072	0.0058	0.0072
	SVR	0.0003	0.0169	0.0108	0.0136
T4 (50%)	ISSA-SVR	0.0002	0.0124	0.0097	0.0130
	SSA-SVR	0.0003	0.0179	0.0135	0.0182
	PSO-SVR	0.0005	0.0219	0.0161	0.0218
	SVR	0.0008	0.0286	0.0216	0.0291
T4 (60%)	ISSA-SVR	0.0001	0.0101	0.0092	0.0124
	SSA-SVR	0.0002	0.0155	0.0125	0.0170
	PSO-SVR	0.0003	0.0186	0.0147	0.0200
	SVR	0.0004	0.0200	0.0143	0.0198
T4 (70%)	ISSA-SVR	0.00004	0.0059	0.0048	0.0066
	SSA-SVR	0.0001	0.0115	0.0094	0.0130
	PSO-SVR	0.0002	0.0128	0.0109	0.0150
	SVR	0.0002	0.0137	0.0105	0.0147

5. Discussion

Accurate estimation of lithium-ion battery SOH is essential for safe and reliable operation. This paper proposes an ISSA-SVR framework that combines convolution-based health indicator extraction, PCA-based dimensionality reduction, and improved sparrow search optimization for SVR parameter tuning. Convolution operations on discharge voltage sequences enable the extraction of nine degradation-related HIs, while PCA reduces redundancy and lowers computational complexity. The ISSA enhances parameter optimization by improving the global search capability and avoiding local optima, thereby strengthening estimation accuracy. Validation on two datasets under different training ratios demonstrates that the proposed method achieves error indicators within 4%, confirming its robustness, stability, and practical potential under diverse aging conditions. Future work will not only focus on validating this methodology on large-format prismatic or pouch cells but will also expand to investigate the model's performance under practical, dynamic operating conditions, including partial charge/discharge cycles, inherent sensor noise, and irregular load profiles.

Author Contributions: R.L.: Methodology, Writing—Original Draft, Conceptualization, Validation. N.H.: Writing—Review and Editing, Investigation, Methodology, Resources, Funding Acquisition. F.C.: Investigation, Supervision, Project Administration. All authors have read and agreed to the published version of the manuscript.

Funding: This research was funded by the National Natural Science Foundation of China (Grant No. 61903291).

Data Availability Statement: The datasets used and/or analyzed during the current study are available from the corresponding author on reasonable request.

Conflicts of Interest: The authors declare that they have no known competing financial interests or personal relationships that could have appeared to influence the work reported in this paper.

References

- Wu, M.; Zhong, Y.; Wu, J.; Wang, Y.; Wang, L. State of health estimation of the lithium-ion power battery based on the principal component analysis-particle swarm optimization-back propagation neural network. *Energy* **2023**, *283*, 129061. [[CrossRef](#)]
- Wang, X.; Wei, X.; Dai, H. Estimation of state of health of lithium-ion batteries based on charge transfer resistance considering different temperature and state of charge. *J. Energy Storage* **2019**, *21*, 618–631. [[CrossRef](#)]
- Ma, Y.; Shan, C.; Gao, J.; Chen, H. A novel method for state of health estimation of lithium-ion batteries based on improved LSTM and health indicators extraction. *Energy* **2022**, *251*, 123973. [[CrossRef](#)]
- Tian, H.; Qin, P.; Li, K.; Zhao, Z. A review of the state of health for lithium-ion batteries: Research status and suggestions. *J. Clean. Prod.* **2020**, *261*, 120813. [[CrossRef](#)]
- Li, Y.; Liu, K.; Foley, A.M.; Zülke, A.; Berecibar, M.; Nanini-Maury, E.; Van Mierlo, J.; Hoster, H.E. Data-driven health estimation and lifetime prediction of lithium-ion batteries: A review. *Renew. Sustain. Energy Rev.* **2019**, *113*, 109254. [[CrossRef](#)]
- Qian, C.; Xu, B.; Xia, Q.; Ren, Y.; Sun, B.; Wang, Z. SOH prediction for Lithium-Ion batteries by using historical state and future load information with an AM-seq2seq model. *Appl. Energy* **2023**, *336*, 120793. [[CrossRef](#)]
- Goh, H.H.; Lan, Z.; Zhang, D.; Dai, W.; Kurniawan, T.A.; Goh, K.C. Estimation of the state of health (SOH) of batteries using discrete curvature feature extraction. *J. Energy Storage* **2022**, *50*, 104646. [[CrossRef](#)]
- Jiang, Y.; Zhang, J.; Xia, L.; Liu, Y. State of health estimation for lithium-ion battery using empirical degradation and error compensation models. *IEEE Access* **2020**, *8*, 123858–123868. [[CrossRef](#)]
- Nazim, M.S.; Rahman, M.M.; Joha, M.I.; Jang, Y.M. An rnn-cnn-based parallel hybrid approach for battery state of charge (SOC) estimation under various temperatures and discharging cycle considering noisy conditions. *World Electr. Veh. J.* **2024**, *15*, 562. [[CrossRef](#)]
- Hu, X.; Che, Y.; Lin, X.; Deng, Z. Health prognosis for electric vehicle battery packs: A data-driven approach. *IEEE/ASME Trans. Mechatron.* **2020**, *25*, 2622–2632. [[CrossRef](#)]
- Li, Q.; Li, D.; Zhao, K.; Wang, L.; Wang, K. State of health estimation of lithium-ion battery based on improved ant lion optimization and support vector regression. *J. Energy Storage* **2022**, *50*, 104215. [[CrossRef](#)]

12. Lyu, Z.; Wang, G.; Tan, C. A novel Bayesian multivariate linear regression model for online state-of-health estimation of Lithium-ion battery using multiple health indicators. *Microelectron. Reliab.* **2022**, *131*, 114500. [[CrossRef](#)]
13. Shim, J.; Kostecki, R.; Richardson, T.; Song, X.; Striebel, K.A. Electrochemical analysis for cycle performance and capacity fading of a lithium-ion battery cycled at elevated temperature. *J. Power Sources* **2002**, *112*, 222–230. [[CrossRef](#)]
14. Galeotti, M.; Cinà, L.; Giannanco, C.; Cordiner, S.; Di Carlo, A. Performance analysis and SOH (state of health) evaluation of lithium polymer batteries through electrochemical impedance spectroscopy. *Energy* **2015**, *89*, 678–686. [[CrossRef](#)]
15. Wei, Z.; Zhao, J.; Ji, D.; Tseng, K.J. A multi-timescale estimator for battery state of charge and capacity dual estimation based on an online identified model. *Appl. Energy* **2017**, *204*, 1264–1274. [[CrossRef](#)]
16. Lyu, C.; Lai, Q.; Ge, T.; Yu, H.; Wang, L.; Ma, N. A lead-acid battery’s remaining useful life prediction by using electrochemical model in the Particle Filtering framework. *Energy* **2017**, *120*, 975–984. [[CrossRef](#)]
17. Li, Y.; Stroe, D.I.; Cheng, Y.; Sheng, H.; Sui, X.; Teodorescu, R. On the feature selection for battery state of health estimation based on charging–discharging profiles. *J. Energy Storage* **2021**, *33*, 102122. [[CrossRef](#)]
18. Xia, F.; Wang, K.; Chen, J. State of health and remaining useful life prediction of lithium-ion batteries based on a disturbance-free incremental capacity and differential voltage analysis method. *J. Energy Storage* **2023**, *64*, 107161. [[CrossRef](#)]
19. Chen, B.; Liu, Y. Data driven-based health prognostics and charge estimation for lithium-ion batteries under varying discharging patterns. *Energy* **2025**, *335*, 137918. [[CrossRef](#)]
20. Zhao, J.; Zhang, X.; Hu, C. Lithium-ion battery State-of-Health estimation using voltage-position encoding CNN and Incremental Capacity Analysis with a novel smoothing parameter selection strategy. *J. Energy Storage* **2025**, *130*, 117296. [[CrossRef](#)]
21. Liu, Y.; Su, Y.; Zhang, S.; Terzija, V.; Cheng, Z. Application of deep learning image recognition for lithium battery State of Health assessment. *Energy Convers. Econ.* **2025**, *6*, 246–255. [[CrossRef](#)]
22. Gu, X.; See, K.W.; Li, P.; Shan, K.; Wang, Y.; Zhao, L.; Zhang, N. A novel state-of-health estimation for the lithium-ion battery using a convolutional neural network and transformer model. *Energy* **2023**, *262*, 125501. [[CrossRef](#)]
23. Bai, T.; Wang, H. Convolutional transformer-based multiview information perception framework for lithium-ion battery state-of-health estimation. *IEEE Trans. Instrum. Meas.* **2023**, *72*, 2523312. [[CrossRef](#)]
24. Zhu, X.; Xu, C.; Song, T.; Huang, Z.; Zhang, Y. Sparse self-attentive transformer with multiscale feature fusion on long-term SOH forecasting. *IEEE Trans. Power Electron.* **2024**, *39*, 10399–10408. [[CrossRef](#)]
25. Zhang, Y.; Li, Z.; Kong, L.; Xu, H.; Shen, H.; Chen, M. Multi-step state of health prediction of lithium-ion batteries based on multi-feature extraction and improved Transformer. *J. Energy Storage* **2025**, *105*, 114538. [[CrossRef](#)]
26. Saha, B.; Goebel, K. *Battery Data Set, NASA Ames Prognostics Data Repository*; NASA Ames: Moffett Field, CA, USA, 2007.
27. Zavala-Mondragón, L.A.; de With, P.H.; van der Sommen, F. A signal processing interpretation of noise-reduction convolutional neural networks: Exploring the mathematical formulation of encoding-decoding cnns. *IEEE Signal Process. Mag.* **2023**, *40*, 38–63. [[CrossRef](#)]
28. Chen, S.; Yu, J.; Wang, S. One-dimensional convolutional auto-encoder-based feature learning for fault diagnosis of multivariate processes. *J. Process Control* **2020**, *87*, 54–67. [[CrossRef](#)]
29. Yang, G.; Wang, J.; Nie, Z.; Yang, H.; Yu, S. A lightweight YOLOv8 tomato detection algorithm combining feature enhancement and attention. *Agronomy* **2023**, *13*, 1824. [[CrossRef](#)]
30. Obregon, J.; Han, Y.R.; Ho, C.W.; Mouraliraman, D.; Lee, C.W.; Jung, J.Y. Convolutional autoencoder-based SOH estimation of lithium-ion batteries using electrochemical impedance spectroscopy. *J. Energy Storage* **2023**, *60*, 106680. [[CrossRef](#)]
31. Karamizadeh, S.; Abdullah, S.M.; Manaf, A.A.; Zamani, M.; Hooman, A. An overview of principal component analysis. *J. Signal Inf. Process.* **2020**, *4*, 173–175. [[CrossRef](#)]
32. Schmid, M.; Endisch, C. Online diagnosis of soft internal short circuits in series-connected battery packs using modified kernel principal component analysis. *J. Energy Storage* **2022**, *53*, 104815. [[CrossRef](#)]
33. Cortes, C.; Vapnik, V. Support-vector networks. *Mach. Learn.* **1995**, *20*, 273–297. [[CrossRef](#)]
34. Ahmed, H.U.; Mostafa, R.R.; Mohammed, A.; Sihag, P.; Qadir, A. Support vector regression (SVR) and grey wolf optimization (GWO) to predict the compressive strength of GGBFS-based geopolymer concrete. *Neural Comput. Appl.* **2023**, *35*, 2909–2926. [[CrossRef](#)]
35. Yuan, X.; Tan, Q.; Lei, X.; Yuan, Y.; Wu, X. Wind power prediction using hybrid autoregressive fractionally integrated moving average and least square support vector machine. *Energy* **2017**, *129*, 122–137. [[CrossRef](#)]
36. Rongyang, W.E.I.; Tian, M.A.O.; Han, G.A.O.; Jianren, P.E.N.G.; Jian, Y.A.N.G. Health state estimation of lithium-ion battery based on TWP-SVR. *Energy Storage Sci. Technol.* **2022**, *11*, 2585.
37. Zhou, S.; Yang, C.; Su, Z.; Yu, P.; Jiao, J. An aeromagnetic compensation algorithm based on radial basis function artificial neural network. *Appl. Sci.* **2022**, *13*, 136. [[CrossRef](#)]
38. Xue, J.; Shen, B. A novel swarm intelligence optimization approach: Sparrow search algorithm. *Syst. Sci. Control Eng.* **2020**, *8*, 22–34. [[CrossRef](#)]

39. Yu, Y.; Gao, S.; Cheng, S.; Wang, Y.; Song, S.; Yuan, F. CBSO: A memetic brain storm optimization with chaotic local search. *Memetic Comput.* **2018**, *10*, 353–367. [[CrossRef](#)]
40. Mirjalili, S. SCA: A sine cosine algorithm for solving optimization problems. *Knowl.-Based Syst.* **2016**, *96*, 120–133. [[CrossRef](#)]
41. Mirjalili, S.; Lewis, A. The whale optimization algorithm. *Adv. Eng. Softw.* **2016**, *95*, 51–67. [[CrossRef](#)]
42. Seyyedabbasi, A. WOASCALF: A new hybrid whale optimization algorithm based on sine cosine algorithm and levy flight to solve global optimization problems. *Adv. Eng. Softw.* **2022**, *173*, 103272. [[CrossRef](#)]

Disclaimer/Publisher’s Note: The statements, opinions and data contained in all publications are solely those of the individual author(s) and contributor(s) and not of MDPI and/or the editor(s). MDPI and/or the editor(s) disclaim responsibility for any injury to people or property resulting from any ideas, methods, instructions or products referred to in the content.